



HAL
open science

The formation of lunar mascon basins from impact to contemporary form

Andrew Freed, Brandon Johnson, David Blair, H. Melosh, Gregory Neumann, Roger Phillips, Sean Solomon, Mark Wieczorek, Maria Zuber

► **To cite this version:**

Andrew Freed, Brandon Johnson, David Blair, H. Melosh, Gregory Neumann, et al.. The formation of lunar mascon basins from impact to contemporary form. *Journal of Geophysical Research. Planets*, 2014, 119 (11), pp.2378-2397. 10.1002/2014JE004657 . hal-02458602

HAL Id: hal-02458602

<https://hal.science/hal-02458602>

Submitted on 26 Jun 2020

HAL is a multi-disciplinary open access archive for the deposit and dissemination of scientific research documents, whether they are published or not. The documents may come from teaching and research institutions in France or abroad, or from public or private research centers.

L'archive ouverte pluridisciplinaire **HAL**, est destinée au dépôt et à la diffusion de documents scientifiques de niveau recherche, publiés ou non, émanant des établissements d'enseignement et de recherche français ou étrangers, des laboratoires publics ou privés.

RESEARCH ARTICLE

10.1002/2014JE004657

Key Points:

- We modeled the evolution of lunar basins from impact to contemporary form
- The evolution of basins results from crater collapse and isostatic adjustment
- Calculations enable estimation of impactor and lunar properties

Supporting Information:

- Readme
- Movie S1
- Movie S2

Correspondence to:

A. M. Freed,
freed@purdue.edu

Citation:

Freed, A. M., B. C. Johnson, D. M. Blair, H. J. Melosh, G. A. Neumann, R. J. Phillips, S. C. Solomon, M. A. Wiczeorek, and M. T. Zuber (2014), The formation of lunar mascon basins from impact to contemporary form, *J. Geophys. Res. Planets*, 119, doi:10.1002/2014JE004657.

Received 5 MAY 2014

Accepted 15 SEP 2014

Accepted article online 19 SEP 2014

The formation of lunar mascon basins from impact to contemporary form

Andrew M. Freed¹, Brandon C. Johnson^{2,3}, David M. Blair¹, H. J. Melosh^{1,2}, Gregory A. Neumann⁴, Roger J. Phillips⁵, Sean C. Solomon^{6,7}, Mark A. Wiczeorek⁸, and Maria T. Zuber³

¹Department of Earth, Atmospheric, and Planetary Sciences, Purdue University, West Lafayette, Indiana, USA, ²Department of Physics, Purdue University, West Lafayette, Indiana, USA, ³Department of Earth, Atmospheric, and Planetary Sciences, Massachusetts Institute of Technology, Cambridge, Massachusetts, USA, ⁴Solar System Exploration Division, NASA Goddard Space Flight Center, Greenbelt, Maryland, USA, ⁵Planetary Science Directorate, Southwest Research Institute, Boulder, Colorado, USA, ⁶Lamont-Doherty Earth Observatory, Columbia University, Palisades, New York, USA, ⁷Department of Terrestrial Magnetism, Carnegie Institution of Washington, Washington, District of Columbia, USA, ⁸Institut de Physique du Globe de Paris, Sorbonne Paris Cité, Université Paris Diderot, Paris CEDEX 13, France

Abstract Positive free-air gravity anomalies associated with large lunar impact basins represent a superisostatic mass concentration or “mascon.” High-resolution lunar gravity data from the Gravity Recovery and Interior Laboratory spacecraft reveal that these mascons are part of a bulls-eye pattern in which the central positive anomaly is surrounded by an annulus of negative anomalies, which in turn is surrounded by an outer annulus of positive anomalies. To understand the origin of this gravity pattern, we modeled numerically the entire evolution of basin formation from impact to contemporary form. With a hydrocode, we simulated impact excavation and collapse and show that during the major basin-forming era, the preimpact crust and mantle were sufficiently weak to enable a crustal cap to flow back over and cover the mantle exposed by the impact within hours. With hydrocode results as initial conditions, we simulated subsequent cooling and viscoelastic relaxation of topography using a finite element model, focusing on the mare-free Freundlich-Sharonov and mare-infilled Humorum basins. By constraining these models with measured free-air and Bouguer gravity anomalies as well as surface topography, we show that lunar basins evolve by isostatic adjustment from an initially subsisostatic state following the collapse stage. The key to the development of a superisostatic inner basin center is its mechanical coupling to the outer basin that rises in response to subsisostatic stresses, enabling the inner basin to rise above isostatic equilibrium. Our calculations relate basin size to impactor diameter and velocity, and they constrain the preimpact lunar thermal structure, crustal thickness, viscoelastic rheology, and, for the Humorum basin, the thickness of its postimpact mare fill.

1. Introduction

Free-air gravity anomalies associated with large impact basins are the most striking and consistent features of the Moon's large-scale gravity field (Figure 1). These anomalies are often found to occur in bulls-eye patterns, in which the central positive anomaly is surrounded by an annulus of negative anomalies, which in turn is surrounded by an outer annulus of positive anomalies. The most prominent central positive anomalies, or “mascons” [Muller and Sjogren, 1968], are associated with impact basins that are generally found on the lunar nearside and that are filled with dense mare basaltic deposits. However, mascons of lesser magnitude are also found in basins that do not possess mare basalt, and the central anomaly has been interpreted as the result of uplift beyond an isostatic state of dense mantle material beneath the basin center [e.g., Neumann *et al.*, 1996; Wiczeorek and Phillips, 1999]. An analysis of gravity and topography measurements suggests that the nearside mare basins would still be mascons even if the gravitational contribution of the mare deposits were removed [Neumann *et al.*, 1996; Wiczeorek and Phillips, 1999]. Thus, an excess of mass at depth characterizes the centers of all large lunar basins. In contrast, the negative free-air anomaly annulus that surrounds these mascon centers represents a deficiency in mass. These annuli are thought to be the result of thickened and deformed crust that was associated with the original processes of impact excavation and collapse and was pushed down below its isostatic level during the impact event [Andrews-Hanna, 2013; Melosh *et al.*, 2013].

The mechanism by which asteroid impact, a process of mass removal that leaves a topographic low, creates basins with excess subsurface mass is one of the oldest puzzles of planetary geophysics. Such a configuration

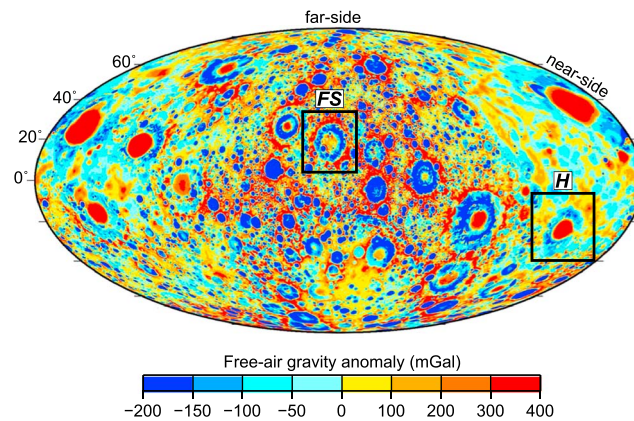


Figure 1. Global free-air gravity field of the Moon, from GRAIL observations [Zuber *et al.*, 2013]. FS: Freundlich-Sharonov and H: Humorum.

is unlikely to have arisen during the collapse of the transient cavity following impact, as this outcome would have required a lithosphere beneath the basin that was capable of supporting a superisostatic load immediately after the impact, at a time when temperatures were sufficiently high to melt both crustal and mantle material. In a recent study that exploited high-resolution gravity measurements from NASA's dual Gravity Recovery and Interior Laboratory (GRAIL) spacecraft [Zuber *et al.*, 2013] and topographic measurements by the Lunar Orbiter Laser Altimeter (LOLA) instrument [Smith *et al.*, 2010],

Melosh *et al.* [2013] showed that the bulls-eye pattern of the free-air gravity anomaly over lunar mascon basins arises as a result of the slow isostatic uplift of the basin that follows excavation and collapse.

In the Melosh *et al.* [2013] study, a hydrocode was first used to model impact excavation and transient crater collapse, and the simulations revealed two important factors that influence the subsequent evolution of these basins. The first is the generation of a thickened crustal collar (~10 km thicker than the surrounding crust), caused by the deposition of ejecta from the transient crater. This thickened crustal section is undermined and downwarped by inward flow of the hot underlying mantle during collapse, producing a subsisostatic collar that is held down by the frictional strength of the shattered but cool crustal material and by the viscoelastic strength of the underlying mantle. The resulting negative density anomaly is consistent with the location (but not the magnitude) of the negative gravity anomaly annulus currently observed in the free-air gravity field. The second factor is that despite a large central melt pool with no strength, the postcollapse basin is held in a subsisostatic state by the strength of the surrounding solid mantle. Thus, the entire impact basin following collapse is in a subsisostatic state, including the inner basin, which we define as the region above the melt pool, and the outer basin, which we define as the region of the thickened crustal collar. Both of these regions are characterized by low elevations following collapse.

Although the crystalline but hot mantle material surrounding the impact basin immediately following impact possesses no long-term strength, its high viscosity relative to that of the surrounding crust implies that a substantial time is required for imposed stresses to relax. The Melosh *et al.* [2013] study utilized finite element models (FEMs) to simulate this relaxation, along with cooling of the melt pool in the tens to hundreds of millions of years following transient crater collapse. The initial conditions for these models were derived from the final conditions of the hydrocode calculations following transient crater collapse. The FEM results showed that the relaxation process enables the basin to rise back toward an isostatic state. Normally, isostatic adjustment cannot lift a region above isostatic equilibrium. However, prior to the uplift in the simulations, the melt pool begins to cool from the surface down. A thick lithosphere thus forms above it and provides a mechanical connection between the inner and outer basins. This lithosphere enables strong isostatic restoring forces acting on the outer basin to raise the inner basin above isostatic equilibrium into a superisostatic state, forming the observed mascon. Although the outer basin also rises, the lithospheric strength of the relatively cool crust and upper mantle prevents it from achieving isostatic equilibrium, leaving it in the configuration observed in the gravity field. The outermost annulus of positive free-air gravity results from uncompensated ejecta deposits located outside the crustal collar, as postulated by Neumann *et al.* [1996] and Wiczorek and Phillips [1999]. Thus, the free-air gravity bulls-eye pattern can be seen as the natural evolution of a large impact basin through four stages: impact excavation, collapse, cooling, and isostatic adjustment.

Here we build on the study of Melosh *et al.* [2013] in several ways. Whereas the earlier study considered only free-air gravity as a constraint on basin structure, we here impose the additional constraints associated with the Bouguer gravity anomaly, i.e., the gravity field corrected for surface topography [Zuber *et al.*, 2013]. The Bouguer gravity field is particularly revealing of contemporary basin structure because it constrains more

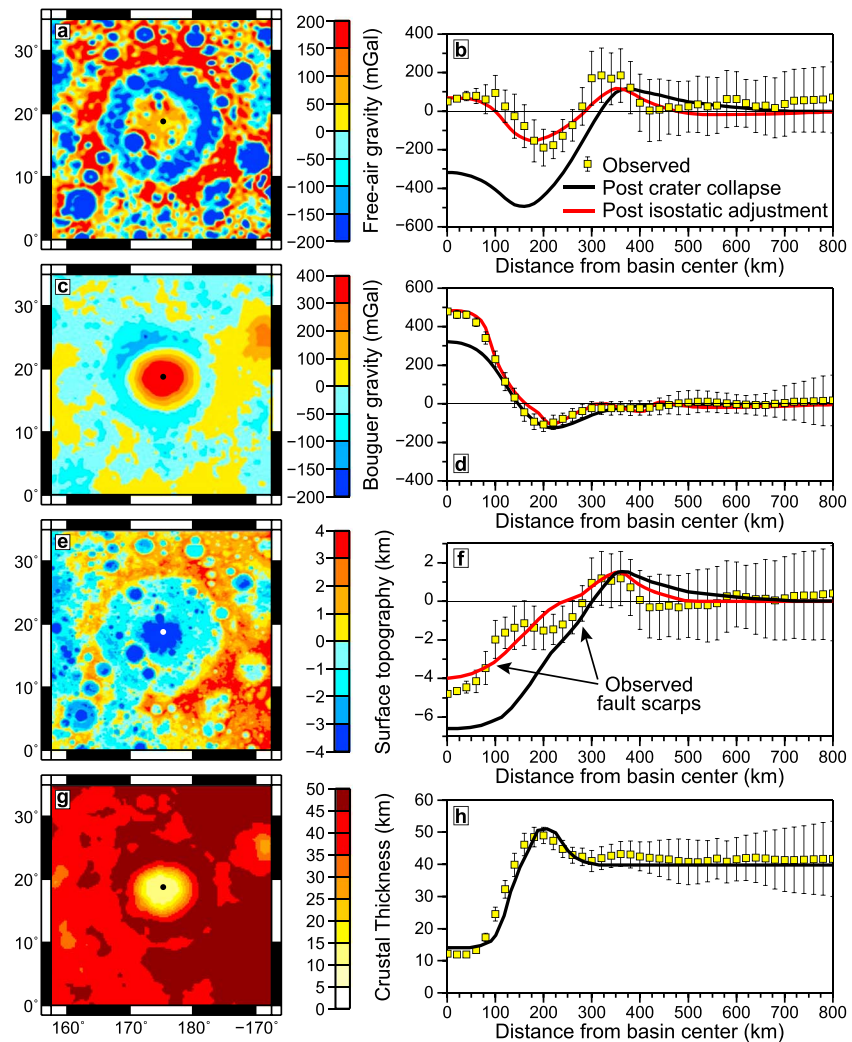


Figure 2. Observational constraints and comparison with best fitting numerical models for the Freundlich-Sharonov basin. (a and b) Free-air and (c and d) Bouguer gravity anomalies from a spherical harmonic expansion of the GRAIL-derived gravity field to degree and order 420 [Zuber *et al.*, 2013] and LOLA-derived topography [Smith *et al.*, 2010]. (e and f) LOLA-derived topography at 16 pixels per degree [Smith *et al.*, 2010]. (g and h) Crustal thickness calculated from GRAIL observations [Wieczorek *et al.*, 2013, model 2]. In Figures 2b, 2d, 2f, and 2g, the black lines show the results of hydrocode simulation for the state of the basin immediately following transient crater collapse, and the red lines show the results of the finite element calculation for the state of the basin after cooling and isostatic adjustment. Observed values are the mean and 1 standard deviation (1σ) variations with radial distance from azimuthal averages of samples taken at 1° intervals around the basin center.

directly the mass anomalies beneath the surface, primarily those associated with variations in crustal thickness. Testing models for basin structure against free-air and Bouguer gravity constraints, as well as inferred crustal thickness and observed topography, greatly reduces nonuniqueness issues and imparts greater confidence in the best fitting model. In addition to applying a broader set of observational constraints, we greatly expand here the range of model parameter space over that treated in the Melosh *et al.* [2013] study, and we explore more fully the influence of each model parameter on basin evolution.

As in the study by Melosh *et al.* [2013], we concentrate on the Freundlich-Sharonov and Humorum basins, because of their similar size but contrast in mare volcanic history. The Humorum basin on the lunar nearside hosts thick deposits of interior mare basalt, whereas the farside Freundlich-Sharonov basin is free of such deposits. As a result of the additional observational constraints imposed in this work compared with the earlier study, we show that the inferred sizes of the impactors responsible for the formation of the Freundlich-Sharonov and Humorum basins are lower by 20% than earlier estimates.

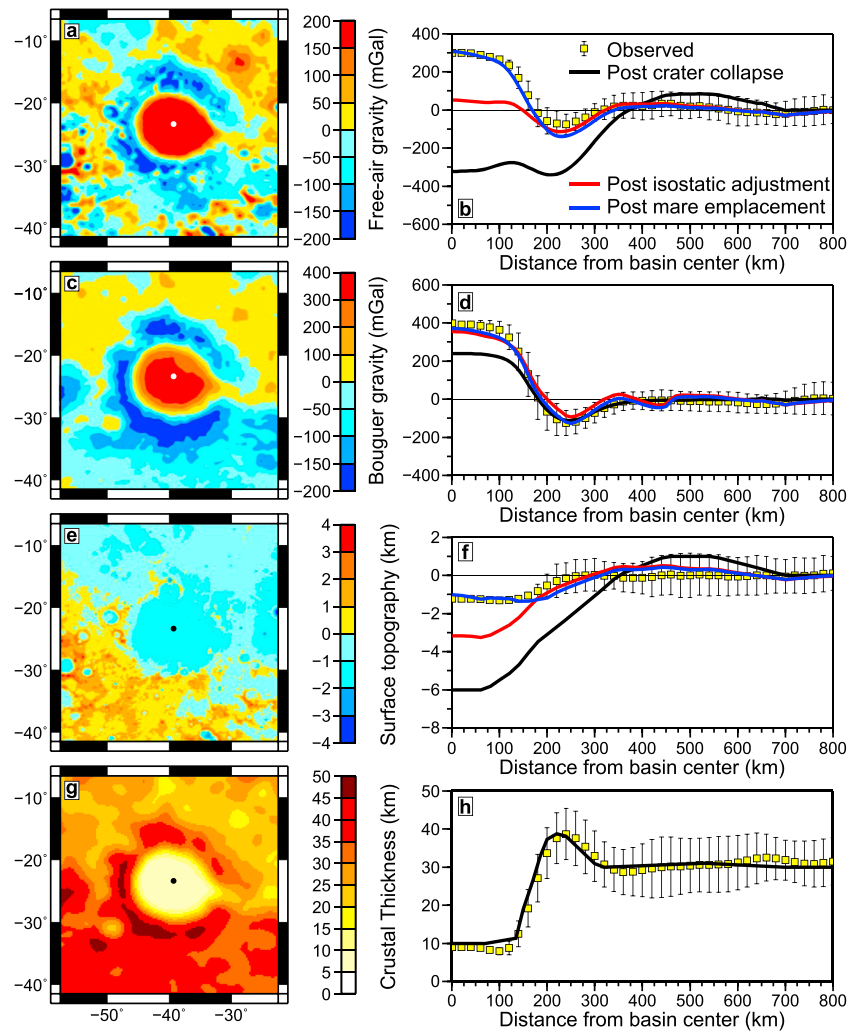


Figure 3. Observational constraints and comparison with best fitting numerical models for the Humorum basin. (a and b) Free-air and (c and d) Bouguer gravity anomalies from a spherical harmonic expansion of the GRAIL-derived gravity field to degree and order 420 [Zuber *et al.*, 2013] and LOLA-derived topography [Smith *et al.*, 2010]. (e and f) LOLA-derived topography at 16 pixels per degree [Smith *et al.*, 2010]. (g and h) Crustal thickness calculated from GRAIL observations [Wieczorek *et al.*, 2013]. In Figures 3b, 3d, 3f, and 3g, the black lines show the results of hydrocode simulation for the state of the basin immediately following collapse, the red lines show the results of the finite element calculation for the state of the basin after cooling and isostatic adjustment, and the blue lines show the results of the finite element model for the state of basin after mare emplacement.

2. Observational Constraints

The free-air gravity and Bouguer gravity anomalies are taken from the spherical harmonic expansions of GRAIL measurements to degree and order 420 (model GL0420A) [Zuber *et al.*, 2013]. Topography data come from LOLA measurements at a resolution of 16 pixels per degree [Smith *et al.*, 2010], and crustal thickness values are taken from an inversion of Bouguer gravity anomaly data [Wieczorek *et al.*, 2013, model 2 in the supporting information]. These data sets are shown in Figures 2 and 3 for Freundlich-Sharonov and Humorum basins, respectively.

The bulls-eye pattern of the free-air gravity anomaly for the Freundlich-Sharonov basin is clearly evident (Figures 2a and 2b). The central mascon is marked by a ~ 100 mGal anomaly, the surrounding crustal collar has a negative anomaly that reaches ~ -200 mGal, and the outer positive annulus reaches values of ~ 200 mGal. The Bouguer gravity anomaly associated with Freundlich-Sharonov basin (Figures 2c and 2d) shows an increase to ~ 500 mGal at the basin center after the removal of the gravitational contribution

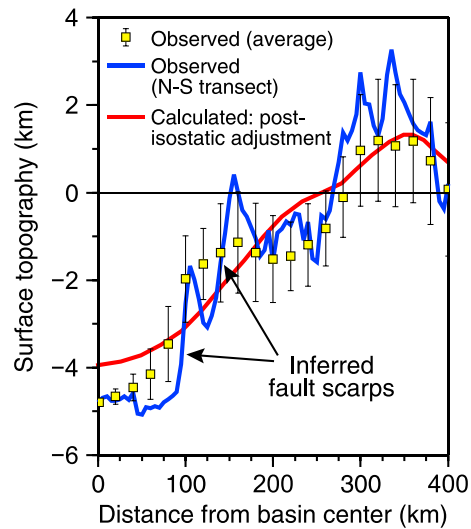


Figure 4. Surface topography determined by LOLA for the Freundlich-Sharonov basin versus that calculated by the finite element model following isostatic adjustment. The blue line shows a northward profile from the center of the basin. Sharp changes in topography at about 100 and 150 km from the basin center are inferred to be fault scarps.

by 1.1 km relative to the absolute lunar datum (a sphere of radius 1737.4 km [Smith et al., 2010]). The topography data have also been azimuthally averaged along a set of concentric small circles centered on each basin mascon in order to arrive at an averaged topographic profile that can be compared with our axisymmetric models (Figures 2b, 2d, 2f, and 2h and 3b, 3d, 3f, and 3h); we took the average of 360 equally spaced elevation points around each circle, and successive circles differ by 5 km ($\sim 6^\circ$) in radius. We have taken 1 standard deviation (1σ) in the distribution of elevations at each radial distance range as a representation of the variation in topography.

The lunar crustal thickness model of Wieczorek et al. [2013] was determined from the Bouguer gravity anomaly field and the observed surface topography, given an inferred crustal density and an assumed mantle density and the depth to the base of the crust beneath the region of the Apollo landing sites inferred from seismic measurements [Wieczorek et al., 2013]. These workers suggested four possible crustal models, for which the global average crustal thickness varied from 34 to 43 km. Figures 2g and 2h show the crustal thickness in the region of the Freundlich-Sharonov basin from model 2 of Wieczorek et al. [2013] with a 34 km average crustal thickness. From this model, we estimate a preimpact crustal thickness of ~ 40 km in the Freundlich-Sharonov region. This same model shows that the modern Freundlich-Sharonov basin has a crustal thickness of ~ 12 km in the inner basin and a crustal collar thickness of ~ 50 km.

The free-air gravity anomaly field for the Humorum basin shows an inner basin mascon of ~ 300 mGal (Figures 3a and 3b), much larger than that of Freundlich-Sharonov because of the presence of interior mare basalt deposits more than 1 km in thickness [Budney and Lucey, 1996]. The influence of the mare infill on surface topography has also been substantial, as the Humorum basin is observed to be just over 1 km deep relative to the surrounding terrain, whereas the Freundlich-Sharonov basin is nearly 5 km deep. At ~ -100 mGal, the peak negative free-air gravity anomaly in the annulus associated with the crustal collar of Humorum is about half the magnitude of that found in Freundlich-Sharonov basin, in part because mare extends outward to cover the inner portion of the crustal collar. The Bouguer anomalies of both basins are very similar, with the Bouguer anomaly of the Humorum inner basin anomaly (Figures 3c and 3d; 400 mGal) modestly less than that in the Freundlich-Sharonov inner basin (500 mGal). The preimpact Humorum basin crustal thickness is inferred to be ~ 30 km, or 20% thinner than that in the Freundlich-Sharonov region, representative of differences in crustal thickness between the nearside and farside of the Moon. The Humorum basin is estimated to have an inner basin crustal thickness of ~ 10 km and a crustal collar thickness

of the topography measured by LOLA (Figures 2e and 2f) under the assumption of an upper crustal density of 2550 kg/m^3 [Wieczorek et al., 2013]. Note the disappearance of the outer positive gravity anomaly in the Bouguer calculation, indicative of a free-air anomaly associated primarily with topography. The Freundlich-Sharonov basin is marked by two sharp changes in topography at ~ 100 and ~ 275 km from the basin center (Figure 2f) that are interpreted to be inward-facing normal fault scarps associated with the multiring structure of this basin. The faults are clearly observable on a north-south cross section of the basin (Figure 4). Our modeling does not treat the complexity of discrete faults, and thus, our results must be interpreted in view of this limitation. Also, for our purposes, variations in the topographic profile are more important than the absolute surface heights.

Thus, we have adjusted the observed surface topography so that zero elevation is defined as the average topographic level well outside the basin. This change in datum was accomplished by uniformly shifting the topographic profile of the Freundlich-Sharonov basin downward by 2.2 km and the Humorum basin upward

Table 1. iSALE Material Input Parameters

Description	Value for Crust	Value for Mantle
Equation of state	ANEOS granite	ANEOS dunite
Melting temperature	1513 K	1373 K
Thermal softening parameter	1.2	1.1
Simon A parameter	1840 MPa	1520 MPa
Simon B parameter	7.27	4.05
Poisson's ratio	0.25	0.25
Frictional coefficient (damaged)	0.71	0.63
Frictional coefficient (undamaged)	1.1	1.58
Strength at infinite pressure	2.49 GPa	3.26 GPa
Cohesion (damaged)	0.01 MPa	0.01 MPa
Cohesion (undamaged)	31.9 MPa	5.07 MPa

of ~40 km (Figures 3g and 3h), less than those of the Freundlich-Sharonov basin by about the same proportion as the differences in the preimpact crustal thickness.

Because of the complexity of surface topography, especially the presence of fault scarps, it is often difficult to assign a particular radius to a basin for purposes of comparison with other features. Here we follow a gravity-oriented convention of assigning basin size on the basis of the radial

distance from the basin center to the inner edge of the thickened crustal collar [Potter *et al.*, 2012a]. With this convention, the Freundlich-Sharonov and Humorum basins are assigned radii of 200 and 215 km, respectively (Figures 2h and 3h).

3. Modeling Approach

Because both the physical processes and time scale that govern impact crater excavation differ from those of cooling and isostatic adjustment, these distinct phases in basin evolution must be simulated by two different numerical codes. We utilized a hydrocode to simulate the influence of high pressures (shock wave) and temperatures on rock deformation in the first few hours following impact and a finite element code to simulate the response to conductive cooling and viscoelastic flow that can take more than a hundred million years to achieve steady state. The key to this two-code approach is to maintain self-consistency by applying the resulting geometry and thermal structure at the end of the hydrocode simulation as initial conditions for the finite element model. This approach enabled us to calculate the evolution of topography and free-air and Bouguer gravity anomalies through the entire evolution of lunar mascon basins from impact to contemporary form, from which we compared candidate models with observational constraints. Both sets of models are axisymmetric, reflecting the fact that lunar basins and their gravity signatures are well approximated by axisymmetry.

3.1. Hydrocode Modeling

We used the iSALE hydrocode [Amsden *et al.*, 1980; Collins *et al.*, 2004; Wünnemann *et al.*, 2006] to simulate the process of crater excavation and collapse. We refer to iSALE as a hydrocode following common usage in the literature for codes that solve problems involving large deformation and finite strain over short time scales. Our objective was to simulate a cratering process that led to a crustal structure consistent with that inferred from gravity and topography measurements [Wieczorek *et al.*, 2013] for the crustal thickness beneath the basin center and the crustal collar. Our modeling suggests that crustal thickness does not markedly vary during post-crater-collapse processes, although we did not consider differentiation of crust as the melt pool cools [e.g., Spudis *et al.*, 2014].

We adopted a two-layer target simulating a gabbroic lunar crust and a dunite mantle, each with pressure- and temperature-dependent densities. We used the ANEOS equation of state for dunite [Benz *et al.*, 1989] to approximate the lunar mantle and impactor and that for granite [Pierazzo and Melosh, 2000] to represent the lunar crust. For both materials, we used the rock-like strength model of Collins *et al.* [2004] and the damage model of Ivanov *et al.* [2010]. An analysis of the GRAIL gravity field and LOLA topography by Wieczorek *et al.* [2013] indicates that the lunar crust is thoroughly fractured, having an average porosity of ~12%. Thus, we treated the lunar crust as a completely fractured rock with a damage parameter = 1, a value indicating that the material is pervasively shattered and thus possesses no cohesive strength, although it still retains frictional strength. As the temperature of a rock-like material increases, the yield stress of the material decreases, making it weaker and more readily deformable. This effect was treated with the rock strength model of Collins *et al.* [2004]. The strength and thermal softening model parameters shown in Table 1 are from Davison [2011] and Potter *et al.* [2012b].

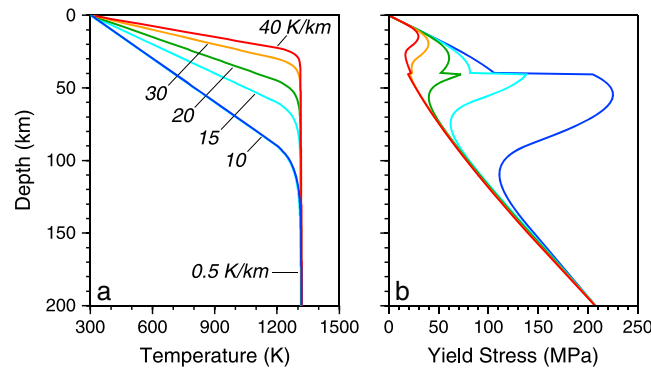


Figure 5. (a) Thermal profiles considered in the hydrocode calculations and (b) corresponding preimpact strength as a function of depth associated with these thermal profiles.

The dependence of material strength on temperature and pressure has the most marked effect on the formation of large impact basins [Ivanov *et al.*, 2010]. In agreement with the results of Ivanov *et al.* [2010], we found that the addition of further weakening by acoustic fluidization did not have a substantial effect on our results. Some form of transient weakening, such as acoustic fluidization, is required to describe fully the collapse of smaller craters [Melosh, 1989]. However, to avoid unnecessary computational expense,

we did not include acoustic fluidization in the models shown here. The behavior of vaporized material does not affect the overall cratering process. Material with a density less than 0.01 kg/m^3 was therefore removed from the calculations to reduce computational cost. The thermal softening model used by iSALE reduces material strength to zero at the melting temperature, taken to be the mantle solidus at a zero-pressure temperature of 1373 K and pressure dependent [Wünnemann *et al.*, 2008]. This approximation is an oversimplification, as material between the liquidus and solidus temperatures should have some shear strength [Stewart, 2011]. Thus, to avoid the presence of abundant supersolidus material, our temperature-depth profiles followed an adiabatic gradient (0.5 K/km) at subsolidus temperatures in excess of 1300 K. With little certainty regarding the temperature-depth profile of the early Moon, we considered thermal gradients in the outermost portions of the Moon ranging from 10 to 40 K/km, from a 300 K surface (Figure 5a). Figure 5b shows the corresponding preimpact strength as a function of depth associated with these thermal profiles for the elastic-plastic rheology adopted in iSALE.

The iSALE model domain extends more than 4000 km in the lateral and vertical directions, with cell dimensions of 1 km \times 1 km near the impact region and cell size gradually increasing beyond this region (Table 2). We did not include the curvature of the Moon, which becomes important when the crater diameter is comparable to the lunar radius of 1737 km [Ivanov *et al.*, 2010]. We assumed a two-layer target and simulated impact into regional crustal thicknesses that varied from 25 to 45 km. Our models consider a range of bolide diameters from 30 to 70 km, and an impact velocity of 15 km/s, the inferred median velocity of lunar impactors [Ito and Malhotra, 2006; Le Feuvre and Wieczorek, 2008, 2011]. There is a trade-off between impact velocity and impactor diameter for a given crater size, in that a larger impactor can compensate for a lower impact velocity and produce the same size crater, and vice versa.

3.2. Finite Element Modeling

To model the postcollapse evolution of the Freundlich-Sharonov and Humorum basins, we used the finite element code Abaqus. The models simulate conductive cooling with changes in temperature-dependent density and viscosity and via viscoelastic flow (isostatic adjustment) caused by pressure and stress gradients associated with the nonisostatic configuration following transient crater collapse. Axisymmetric models of the basins were taken from the geometry of the final state (postcollapse) of the hydrocode simulations. As

each hydrocode run leads to a variation in the postcollapse geometry and thermal structure, we developed a new FEM associated with each hydrocode model to preserve self-consistency. We used primarily linear quadrilateral elements with a few triangular elements to reduce element distortion

Table 2. iSALE Model Description

Description	Value
Size of high-resolution cell	1 km
Number of high-resolution cells, horizontal direction	400
Number of high-resolution cells, vertical direction	400
Impact velocity	15 km s^{-1}
Surface gravitational acceleration	1.62 m s^{-2}

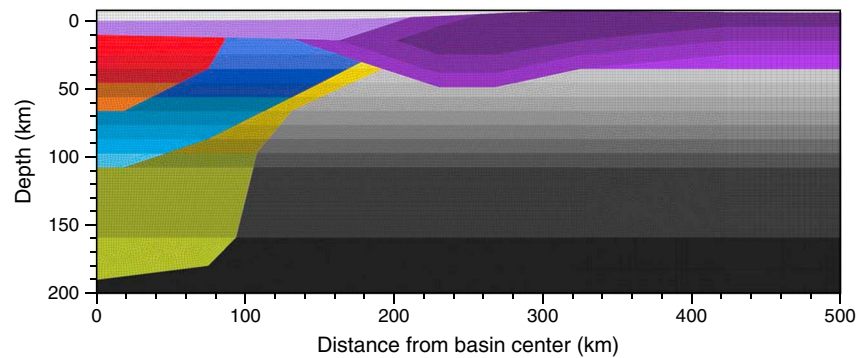


Figure 6. Inner portion of a representative finite element grid of the Freundlich-Sharonov basin used in this analysis. Colors show regions of shared initial density and thermal structure. The purple hues represent crustal material, the grey hues represent mantle material, the white section at the top corresponds to empty space, and all other colors represent the melt pool.

in geometrically complex regions. A portion of a typical Freundlich-Sharonov FEM mesh is shown in Figure 6. The full models extend laterally to 2000 km from the basin center and 800 km in depth; models have $\sim 1 \text{ km} \times 1 \text{ km}$ element resolution within 400 km of the impact site, and cell size gradually increases outward and downward. Resolution tests showed that a more detailed mesh did not substantially influence model results. Far-field boundaries are fixed but are at sufficient distance so as not to influence model results.

FEM calculations followed a four-step process, with the thermal evolution developed in the first two steps and the mechanical evolution developed in the second two steps. The decision to decouple the thermal and mechanical evolution was made to reduce run times. Sample runs from a fully coupled analysis showed no marked difference in model results because viscoelastic flow is limited to only a few kilometers; i.e., no significant advection occurs in the analysis. In the first step, the background (preimpact) temperature gradient consistent with that assumed for the hydrocode (see the discussion of hydrocode results below) was developed from a combination of thermal boundary conditions (300 K at the surface and 1346 K at 800 km depth) along with radiogenic heat generation in the upper 50 km. In this step, temperature varies only as a function of depth, and the model was run with the applied boundary conditions until a steady-state temperature was achieved. In the second step, the post-crater-collapse thermal structure from the hydrocode was applied as an initial condition in the FEM in regions perturbed by the impact, whereas the rest of the model began with the steady-state thermal structure from the first step. The heat production applied in the first step was also applied in the second step to maintain the steady-state background thermal structure. From these initial conditions, a conductive heat transfer calculation was performed until the entire model cooled to the preimpact thermal structure from the first step. This second step provided the thermal evolution that was utilized in the subsequent viscoelastic relaxation calculation. For our step 1 and step 2 thermal models, we assumed a specific heat of $1000 \text{ J kg}^{-1} \text{ K}^{-1}$ and a thermal conductivity value of $2.5 \text{ W m}^{-1} \text{ K}^{-1}$, although these parameters do not influence the final calculated thermal structure.

The third modeling step calculates the overburden pressure within each element in order to generate a lithostatic prestress as an initial condition for the subsequent cooling and viscoelastic calculations. Without this prestress, the application of gravity would cause the mesh to self-compress. The prestress calculation requires that the initial density structure be determined. Although it would be more self-consistent to utilize the density structure from the hydrocode results, the equation of state used by the hydrocode does not take into account the effect of the change in phase from solid to melt on the density structure. The FEM calculations must consider the influence of this phase change on density as the melt pool cools.

We developed a phase-sensitive expression for the density of the lunar mantle for the FEM calculation. The melt pool beneath a large impact basin is a poorly understood mixture of the Moon's upper mantle, overlying crust, and impacting projectile. The impact melts nearly all of the material directly beneath the "footprint" of the projectile, including nearly all of the crust in this area and a hemispherical volume of the upper mantle. We approximated the uncertain composition of this mixture by the bulk composition of the Moon. This bulk composition approximates the re-mixing of melted crust and upper mantle, as well as qualitatively including an injection of more primitive material from the projectile itself. Thus, starting with the bulk silicate composition of

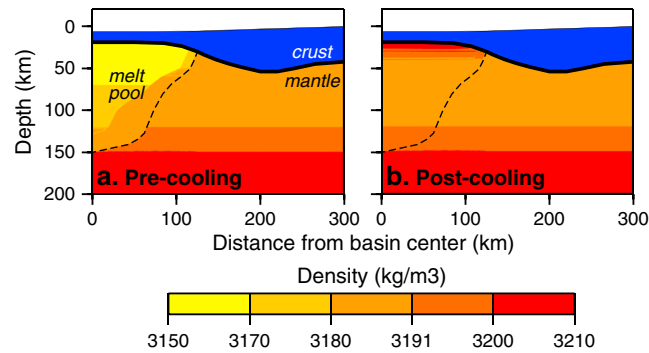


Figure 7. An example of an (a) initial precooling and (b) final postcooling density structure for a typical Freundlich-Sharonov finite element calculation. The color scale used to highlight density changes in the mantle does not show the modest density changes in the crust that also occur during cooling.

were assumed to be carried in anorthite whereas at greater depths, they were assumed to be present in garnet. The density of each mineral was computed as a function of pressure and temperature. Melt densities were computed from the composition and the partial molar properties of each oxide component. The details of this calculation were discussed by *Melosh et al.* [2013] (see their supporting information).

This density calculation was used to determine the initial (post-collapse/precooling) FEM density structure (Figure 7a) for the prestress (overburden) and the density structure after cooling (Figure 7b). Note that the mantle material in the impact region is less dense than material at similar depths outside the basin because of elevated temperatures. After cooling, mantle densities are assumed to be once again purely depth dependent. We used the precooling density structure to calculate overburden pressures in each element. By subtracting the overburden outside the basin at a given depth from each element within the basin, the resulting pressure difference (Figure 8) reveals the basin's deviation from an isostatic state. Low elevation leads to low subsisostatic pressure beneath the inner basin. This effect is compensated at ~45 km depth by shallow mantle (Figure 8). However, at greater depth, mantle density remains lower than normal because of elevated temperature, and the structure at such depths is again in a subsisostatic state. Subsistostatic forces are greatest beneath the crustal collar ~200 km from the basin center as a result of a combination of a thicker crust, held down by frictional strength, and low surface elevation. Outside the basin, pressures become superisostatic as a result of ejecta loading. Higher pressures well outside the basin will drive viscous mantle toward the basin center and will induce uplift of the basin floor and crustal collar. In contrast, mantle will flow away from the higher pressures beneath the outer ejecta blanket, inducing subsidence.

The final modeling step is a time-dependent calculation of thermal contraction due to cooling and viscoelastic flow caused by the aforementioned pressure gradients until steady-state conditions in thermal structure,

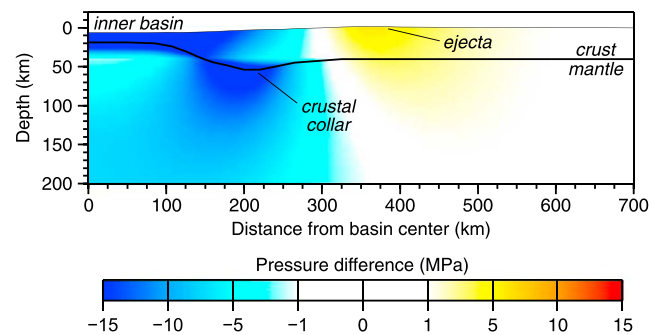


Figure 8. Overburden pressure differences between regions external to the basin (beyond 600 km from the basin center) and those internal to the basin following transient crater collapse. The cool colors denote regions of subsisostatic loading, whereas the warm colors denote regions of superisostatic loading.

the Moon [*Taylor, 1982*], we estimated the melt density from the partial molar properties of each oxide component, following the prescription of *Bottinga and Weill* [1970] with the data of *Lange and Carmichael* [1990]. The densities of the solid phases were computed from our assumed bulk composition with a normative procedure by which we distributed the oxide components among a suite of common minerals that depend on the pressure stability range of each mineral. Olivine and pyroxene are the dominant minerals at all pressures, but at depths less than 150 km in the Moon, calcium and aluminum

density structure, and deformation are achieved. The initial conditions for this step include the geometry and temperature at the end of transient crater collapse from the hydrocode run, the associated density structure as calculated from the phase-sensitive expression derived above, the lithostatic prestresses from step 3, and an initial temperature-dependent viscoelastic structure. The evolution of the thermal structure in this calculation follows the conductive cooling solution determined in the second step.

In order to track the evolution in the density structure from the precooling

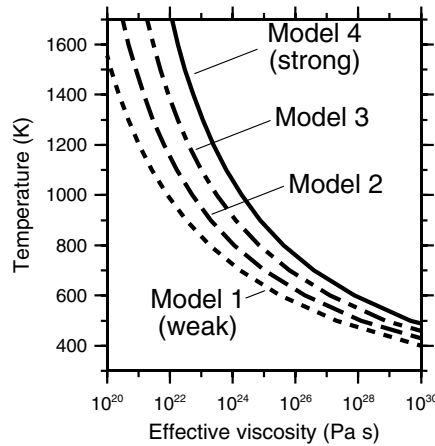


Figure 9. Temperature-dependent viscosity models used in the finite element analysis. Viscosity is taken from equation (1) and parameters associated with dislocation creep of dry Maryland diabase [Mackwell *et al.*, 1998] (see text).

configuration (Figure 7a) to the postcooling configuration (Figure 7b), we must assign the appropriate coefficients of thermal expansion for each element. This step was accomplished with the equation, $\alpha_v = \Delta\rho/(\rho_i \Delta T)$, where α_v is the volumetric coefficient of thermal expansion (with units of K^{-1}), $\Delta\rho$ is the density change experienced by each element during cooling (kg/m^3), ρ_i is the initial density of each element (kg/m^3), and ΔT is the change in temperature (K) experienced by each element. Changes in density associated with changes in pressure are automatically incorporated by the continuum equations utilized in the FEM solver. This approach guarantees that both the initial and final density structures will be consistent with the changes in pressure and temperature experienced by each element during cooling and isostatic adjustment.

A temperature-dependent rheology is critical for this calculation in order to simulate the strengthening of viscous material as it cools, enabling the growth of an elastic lithosphere over the melt pool. Rheology also controls the overall rate of isostatic adjustment. We used a Newtonian approximation with a uniform strain rate field derived from the temperature-dependent creep data of dry Maryland diabase [Mackwell *et al.*, 1998],

$$\eta = \dot{\epsilon}^{(1-n)/n} e^{Q/(nRT)} / (2A^{1/n}), \quad (1)$$

where η is the viscosity, $\dot{\epsilon}$ is the strain rate, n is the strain (or stress) exponent, Q is an activation energy, R is the universal gas constant, T is absolute temperature, and A is an experimental constant. For dry Maryland diabase, $A = 8 \text{ MPa}^{-4.7} \text{ s}^{-1}$, $Q = 485 \text{ kJ/mol}$, and $n = 4.7$ [Mackwell *et al.*, 1998].

Our approach to modeling the rheology of the mantle is by implementing equation (1) for a uniform assumed strain rate, which allows this parameter to be used to shift uniformly the viscosity structure to be stiffer or weaker while maintaining its temperature dependence. Temperature-dependent viscosity structures for four assumed strain rates (10^{-14} , 10^{-15} , 10^{-16} , and 10^{-17} s^{-1} ; models 1–4, respectively) are shown in Figure 9. Model 1 is a relatively fluid rheology for which mantle viscosities (over the temperature range 1200–1350 K) remain below 10^{21} Pa s . Model 4 is a relatively stiff rheology for which mantle temperatures imply viscosities greater than 10^{23} Pa s . We interpret the persistence of the thickened crustal collar to contemporary times as evidence that the entire crust is viscously strong. Thus, we do not consider a separate flow law for the crust. Instead, we assign the same temperature-dependent rheology, which causes the crust to be stronger than mantle material because of lower temperatures. Strain rates in the lunar mantle lower than the range considered would correspond to a higher viscosity than treated here. In contrast, the lunar mantle may have been weakened by water or other volatiles relative to the flow law for dry diabase, which would have led to a lower viscosity [cf. Evans *et al.*, 2014]. These possibilities highlight the large uncertainty in lunar mantle rheology and serve to reinforce the view that the assumed strain rates should be regarded simply as proxies that enable consideration of a large range of possible viscosity structures in the modeling.

Even with the simplified approach to modeling temperature-dependent rheologic structure, simulating a very low viscosity ($<10^{19} \text{ Pa s}$) for melt (temperatures greater than 1500 K) is problematic for model calculations because of the required short time steps (i.e., prohibitively long run times) and numerical instabilities. However, testing models with viscosities as low as 10^{18} Pa s for the hotter regions of the melt pool revealed that the viscosity of these regions does not influence model results as long as the initial melt pool viscosity is at least a factor of 10 less (i.e., is much weaker) than the surrounding solid regions. From temperature differences alone, material within the melt pool is sufficiently fluid compared with the surrounding mantle and crustal lid that it does not require a separate flow law that incorporates a very low-viscosity liquid phase. Our lower cutoff for viscosity was thus set to 10^{19} Pa s .

For the Humorum basin, the finite element model must also simulate a final mare-infilling phase and associated subsidence. This step was accomplished by generating a new Humorum FEM with the same geometry and rheological structure as the final state following cooling and isostatic adjustment but with a new set of elements that represent mare basalt deposits within the basin. We assumed that the mare basalt material has an average density of 3200 kg m^{-3} on the basis of observations of mare basalt samples that vary in bulk density from 3000 to 3300 kg m^{-3} and in grain density from 3300 to 3500 kg m^{-3} [Kiefer *et al.*, 2012]. We also assumed that the mare deposits in a given basin were emplaced as a single unit and the mantle then relaxed to steady state, simulating the flexure that results from surface loading. Although this approach is not appropriate for simulating the evolution of basin faulting on time scales less than or comparable to the interval during which mare volcanism was active in this region, it should be sufficient to simulate the final geometric structure that controls the topographic and gravitational signature of the basin. The depth and extent of mare fill within the basin were adjusted as model parameters to match gravity and topographic observations. Predicted Bouguer gravity anomalies were determined by subtracting the free-air gravity field of the final deformed configuration from the free-air gravity field of the modeled preimpact configuration and by assigning an upper crustal density of 2550 kg m^{-3} to the topography, following Wieczorek *et al.* [2013]. All gravity anomalies were computed at an altitude of 10 km above the lunar datum to avoid dealing with artifacts that arise when the elevation exceeds the height of the surface on which the anomalies are evaluated. The GRAIL gravity field, however, has been continued downward to the lunar datum. Tests were performed to confirm that the calculated gravity anomalies at altitudes of 0 and 10 km do not differ substantially.

4. Results

4.1. Hydrocode Model Results

The main parameters controlling basin geometry following impact and transient crater collapse are the size and velocity of the impactor, the thickness of the preimpact crust, and the preimpact temperature as a function of depth [Ivanov *et al.*, 2010; Potter *et al.*, 2012b; Miljković *et al.*, 2013]. We sought a combination of these factors that would lead to the observed variation of crustal thickness with distance from the basin center for the Freundlich-Sharonov and Humorum basins, as shown in Figures 2h and 3h, respectively. We found that the crustal structure of both basins is best matched by an impactor of about 40 km in diameter striking at 15 km/s , with a preimpact lunar thermal gradient of 30 K/km (until a depth at which an adiabat is reached), and preimpact crustal thickness values of 40 and 30 km for the Freundlich-Sharonov and Humorum basins, respectively. Previous models [Ivanov *et al.*, 2010; Potter *et al.*, 2012b] predicted that basins the size of Freundlich-Sharonov and Humorum should have zero crustal thickness at the basin center (i.e., completely exposed mantle). This prediction is at odds, however, with the GRAIL-derived crustal thickness model of Wieczorek *et al.* [2013]. In addition to incorporating more recent estimates for preimpact crustal thickness [Wieczorek *et al.*, 2013], we describe a mechanism by which a cap of crustal material can cover the center of an impact basin.

A time series showing the evolution of the Freundlich-Sharonov basin from shortly after impact to steady state following transient crater collapse is shown in Figure 10 (an animation of this process is included in the supporting information). These panels show how crustal and thermal structures evolve during the first few hours following impact. Seven minutes after impact, the ejecta curtain has moved beyond the rim of the transient crater, which has begun to collapse (Figure 10a). For the 40-km -diameter dunite impactor, the maximum depth of excavation is $\sim 34 \text{ km}$, and although there may be a weak dependence on crustal thickness, the excavation depth is independent of thermal gradient [Potter *et al.*, 2013]. Thus, the crust is nearly completely excavated as the transient crater forms. The ejecta curtain then begins to cover the outer basin, serving to thicken the crust. At 10 min , the ejecta curtain has reached more than 300 km from the basin center, which has rebounded to generate a transient central uplift, and the crustal material from outside the basin is beginning to slide inward as the transient crater continues to collapse (Figure 10b). The inner part of the crust also bends downward into the transient cavity at this time, plastically deforming the shattered (but still cool and having frictional strength) crust, a deformation that will later hold the low-density crust down against the isostatic forces that tend to uplift it. At 13 min , the central uplift is near its maximum height of 100 km above the lunar surface, ejecta is being emplaced more than 500 km from the basin center, and crustal material continues to move downward and inward toward the basin center (Figure 10c). At 23 min after impact, the central uplift has collapsed down to a depth of 25 km below the original surface, and ejecta-thickened crust

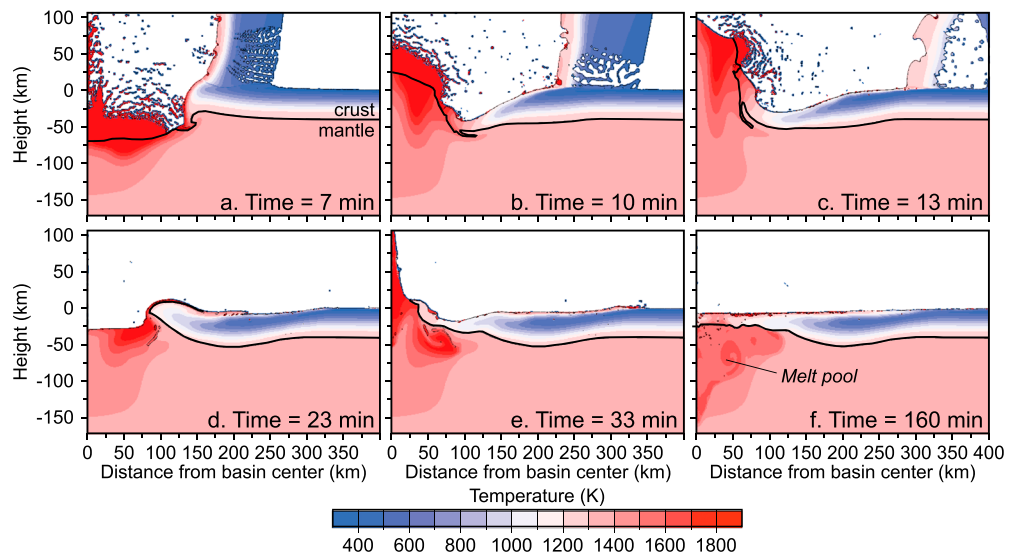


Figure 10. Hydrocode time series showing the formation of the Freundlich-Sharonov basin by the impact of a 40-km-diameter bolide striking vertically at a velocity of 15 km/s into a target with a 40-km-thick crust and a shallow thermal gradient of 30 K/km. Material is colored according to its temperature as indicated by the color bar. The interface between crustal and mantle material is denoted by a black line.

continues to move inward toward the basin center (Figure 10d). At this time, mantle material is completely exposed in the center of the basin. The collapse of the central uplift has also caused warm crustal material, originally derived from the base of the crust, to flow outward over the surface of the crust, contributing to crustal thickening. There are pools of melted mantle material that end up on the surface of the crust from this collapse of the central uplift, which has also created a large bulge of material ~ 100 km from the basin center (Figure 10d). It is the subsequent collapse of this bulge that creates a secondary central uplift and causes a thin layer of crustal material to move inward (Figure 10e). Outside the transient cavity, the ejecta-thickened crust has stabilized, defining a crustal collar about 200 km from the basin center (Figure 10e).

By 160 min after impact, the secondary central peak has collapsed, and the dynamics of transient crater collapse have dampened nearly to steady state, with the basin center settling at a depth of ~ 6.5 km below the preimpact surface (Figure 10f). The crust has moved inward to cover the inner basin completely. The predicted crustal structure for the Freundlich-Sharonov basin at the end of transient crater collapse has an inner basin crustal cap of ~ 14 km thickness formed primarily by inward lateral displacement of the crust and a predicted crustal collar 51 km thick and centered at ~ 200 km from the basin center. The extra thickness of the collar region is primarily the result of ejected crustal material from within the basin (black line in Figure 2h). This crustal thickness is in good agreement with that inferred from gravity and topography observations. Note that the centerline of the preimpact crust has been strongly downwarped, reflecting the plastic deformation that occurred as the crust slid inward into the transient crater cavity.

A similar process of impact excavation and collapse is calculated to have occurred for the Humorum basin, with the only difference being an initially thinner crust in the Humorum region (30 km) than for the Freundlich-Sharonov region (40 km). Figure 11a shows the final, postcollapse geometry, and thermal structure of Humorum calculated by the hydrocode model. The resulting crustal cap at the basin center is 10 km thick, and there is a 40 km thick crustal collar located ~ 215 km from the basin center (black line in Figure 3h), in good agreement with that inferred from gravity and topography observations.

The inner crustal caps of the Freundlich-Sharonov and Humorum basins cover a melt pool, denoted by temperatures above ~ 1400 K, that is just below the crust and extends horizontally more than 100 km from the basin center and vertically to a depth of 150 km at the basin center (Figures 10e and 11a). Subsequent analysis shows that the crustal caps above the melt pools as well as the thickened crustal collars are in a subsisostatic state following transient crater collapse. Such a state requires strength to resist isostatic forces that work to drive the basin upward toward isostatic equilibrium. Because the melt pool has no strength, it was generally thought that the inner basin would not be out of isostatic equilibrium following transient crater collapse. However, in order for

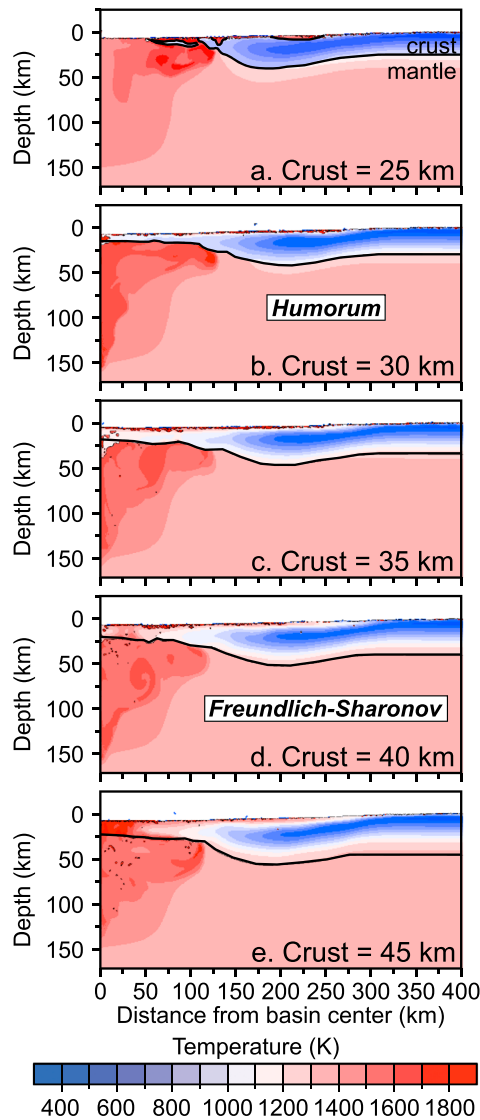


Figure 11. Hydrocode predictions of postcollapse basin structure following a 40-km-diameter impactor striking vertically at a velocity of 15 km/s into a target with a thermal gradient of 30 K/km as a function of the assumed preimpact crustal thickness. Other conventions as in Figure 10.

crustal cap is present), whereas for an impact into a target with a crustal thickness of 45 km (Figure 11e), the crustal cap is ~20 km thick. The crustal cap is also hotter as the preimpact crustal thickness increases. The thickened cap and increased temperature are the result of a hotter and weaker lowermost preimpact crust that more readily migrates toward the basin center during collapse. Another important effect contributing to the increased temperature of the thicker crustal caps is the presence of more shock-heated crustal material when the preimpact crust is thicker, a result of the geometry of the excavation zone and contours of peak shock pressure [Melosh, 1989]. At the center of the basin, formed in crust initially 45 km thick (Figure 11e), molten crust lies atop molten mantle. This partitioning can be regarded as a proxy for the differentiation of impact melt.

The effect of thermal gradient on postimpact basin structure is shown in Figure 12. As the thermal gradient increases, the depth of the basin decreases from 10 km at 15 K/km (Figure 12a) to 5 km at 40 K/km (Figure 12d). Although not shown in Figure 12, the 10 K/km thermal gradient yields a basin 18 km deep. Lower thermal gradients lead to a deeper basin because colder material is stronger and thus better

the melt pool to rise, the surrounding solid mantle must rise as well. Though relatively hot, this mantle nevertheless has sufficient strength to support the subsostatic load on the short time scales treated in the hydrocode. Because of its viscous strength, the mantle requires time to relax as shown in our FEM results. In addition, though extensively damaged, the crust maintains frictional strength that resists isostatic forces. Combined, the strength of the crustal and mantle material surrounding the melt pool is sufficient to hold them in a subsostatic state through the time frame of transient crater collapse (several hours). Given time, these isostatic forces will indeed cause the basin to rise as the mantle flows inward, although this process—treated in our FEM calculations—takes millions of years. The cool crust, however, never relaxes and retains to the present the annular negative gravity anomaly in its subsostatic state.

The good fit of the predicted and inferred crustal structures of the Freundlich-Sharonov and Humorum basins was achieved through an exploration of the space of model parameters, including the preimpact crustal thickness, the diameter of the bolide, and the preimpact thermal gradient. Figure 11 shows the results of hydrocode calculations of post-collapse geometry and thermal structure as a function of preimpact crustal thickness. The main influence of crustal thickness is that thicker preimpact crust leads to a thicker crustal cap. In part, this outcome is a consequence of the relative magnitudes of depth of excavation and crustal thickness. Another complementary effect is that for a thicker crust, the base of the crust is weaker for a given thermal gradient. For a 40-km-diameter dunite impactor striking at 15 km/s, the maximum depth of excavation is ~34 km [Potter *et al.*, 2013], but the case with 30-km-thick crust still produces a crustal cap (Figure 11b). For an impact into a target with 25-km-thick crust (Figure 11a), there is fully exposed mantle material at the center of the basin (i.e., no

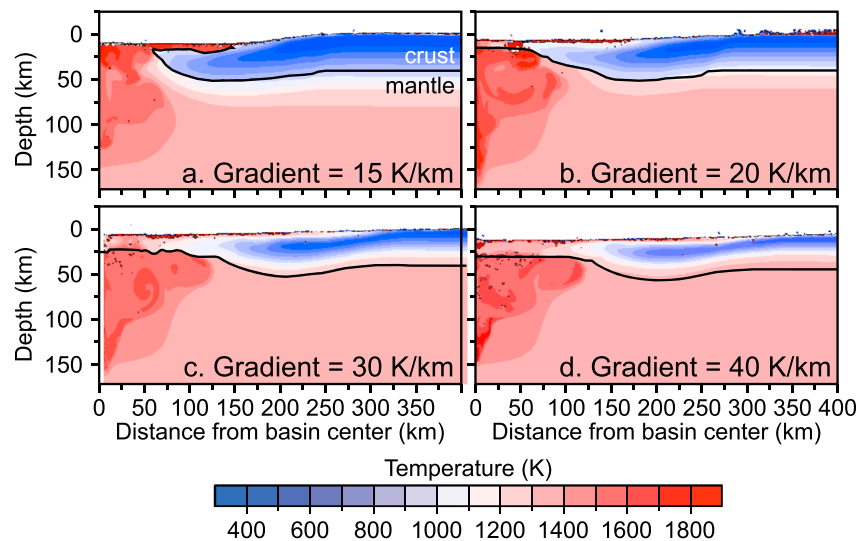


Figure 12. Hydrocode predictions of postcollapse basin structure following a 40-km-diameter impactor striking vertically at a velocity of 15 km/s into a target with a 40-km-thick crust as a function of the assumed lunar thermal gradient. Other conventions as in Figure 10.

able to support greater subisostatic loads and prevent the basin floor from rising. Low thermal gradients also lead to a thinner crustal cap beneath the inner basin, because cooler crustal material is too strong to flow readily toward the basin center during collapse. For the 15 K/km thermal gradient, crustal material is not able to migrate to the inner basin sufficiently to form a crustal cap, although some underresolved crustal material is caught in the backflow from the collapse of the transient central uplift (Figure 12a), but the volumetric significance of such material is not clear. To show the difference between a model that produces a crustal cap and one that does not, we have included animations for the 15 and 30 K/km thermal gradients in the SOM. Thermal gradients of 20–40 K/km lead to crustal caps 10–20 km thick, respectively (Figures 12b–12d).

As the thermal gradient increases and material becomes weaker, the rim position (highest surface elevation) moves outward from the basin center and a prominent thickened crustal collar develops. For the 15 K/km thermal gradient (Figure 12a), the rim is located ~330 km from the basin center (Figure 12a), whereas the rim is located ~390 km from the basin center for the 40 K/km case (Figure 12d), more in line with contemporary topography. Higher thermal gradients also lead to a thicker and more distinct crustal collar (more pronounced curvature) located farther from the basin center. A 30 K/km gradient produces a crustal collar centered at ~200 km from the basin center. This similarity in shape to that defined by gravity observations was the primary reason that this higher value was chosen as the best fitting thermal gradient. Changes to the mantle adiabat, here assumed to be 1300 K, could also give different results. Other models that use mantle adiabats at or above the melting temperature result in more mantle flow and less inflow of crustal material [Potter *et al.*, 2012b], resulting in shallower craters that do not exhibit a crustal cap. The current version of iSALE adopts a rock-like elastic-plastic rheology [Collins *et al.*, 2004]. The addition of a more complete viscoelastic-plastic rheology and inclusion of a strain-rate-dependent viscosity may substantially reduce the short-term strength of the hot mantle material. Similarly, the addition of any other weakening mechanism, such as acoustic fluidization [Melosh, 1989], would also tend to decrease the thermal gradient required to match the observed gravity field characteristics. It is also worth noting that we did not include porosity compaction or dilatant bulking, either of which could produce changes in the predicted basin structure.

The effect of impactor size on postcollapse basin structure for a fixed (vertical) impact velocity of 15 km/s is shown in Figure 13. As expected, as the impactor size increases, the melt pool increases in size with respect to the size of the transient crater [Melosh, 1989]. The position of the crustal collar also moves outward as the impactor size increases [Potter *et al.*, 2012b]. The degree of thickening in the crustal collar increases from 8 km of thickening for a 30-km-diameter impactor to 13 km of thickening for a 70-km-diameter impactor. This thickening occurs primarily as a result of the increasing thickness of the ejecta curtain with larger impactors. The

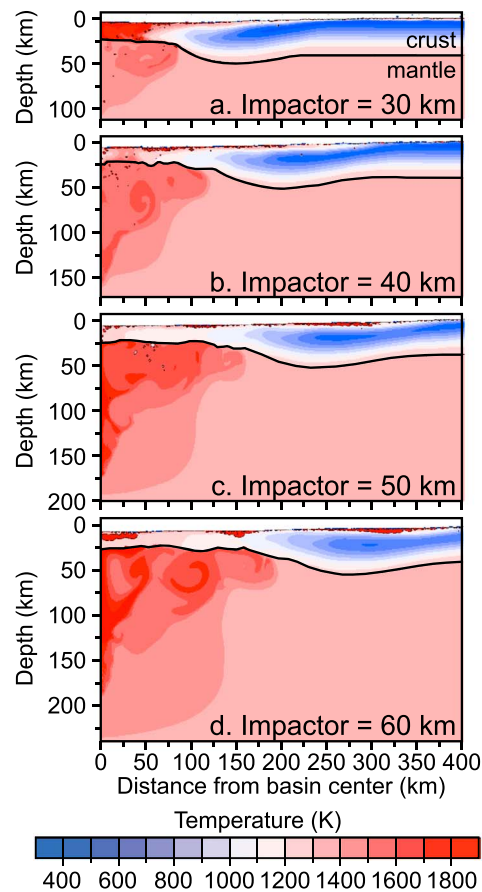


Figure 13. Hydrocode predictions of postcollapse basin structure following an impactor striking vertically at a velocity of 15 km/s into a target with a 40-km-thick crust and a thermal gradient of 30 K/km as a function of the diameter of the impactor. Other conventions as in Figure 10.

substantially thinner than has been inferred here, then a model with a smaller impactor, or a thinner preimpact crust, or a lower thermal gradient would be required. However, such models would have led to inconsistencies with other constraints. For example, a smaller impactor would have placed the thickened crustal collar too close to the basin center, a thinner preimpact crust would have required an average global crust thinner than the minimum (34 km) suggested by global observations of gravity and topography [Wieczorek *et al.*, 2013], and a cooler preimpact thermal gradient would not have led to a sufficiently thickened crustal collar. Thus, we conclude that at least for these two lunar basins, there was only minimal crustal differentiation during cooling of the melt pool.

For the Freundlich-Sharonov and Humorum hydrocode models that produce the postcollapse crustal structure in best agreement with that inferred from gravity and topography observations (Figures 10f and 11a, respectively), we calculated the free-air and Bouguer gravity anomalies and the surface topography from the models. These results were then compared with the observations (right columns of Figures 2 and 3). The Freundlich-Sharonov and Humorum models greatly underpredict the free-gravity anomalies throughout the basin, including the crustal collar, and they overpredict the free-air anomaly outside the basin in the vicinity of the outermost ejecta (Figures 2b and 3b). This result is consistent with an overprediction of the depth of the contemporary basins and ejecta topography outside the basin (Figures 2d and 3d). The Bouguer gravity anomaly is underpredicted in the inner basin but is in fairly good agreement in the vicinity of the crustal collar and ejecta region outside the basin (Figures 2f and 3f). These inner basin differences are the result of differences in the shape of the basin floor, in that the contemporary shape is flatter than that predicted by the hydrocode following transient crater collapse. These comparisons clearly show that the Freundlich-Sharonov

basin depth and rim position increase with increasing impactor size from a 4 km deep basin with a rim located ~300 km from the basin center for a 30-km-diameter impactor to an 8-km-deep basin with a rim located ~650 km from the basin center for a 70-km-diameter impactor. In contrast, the thickness of the crustal cap is reduced with increasing impactor size. This effect is due to the greater distance that crustal material must migrate to reach the basin center, which causes the crustal layer to be more extended. For sufficiently energetic impacts, the solidified melt pool at the basin center will likely be completely exposed regardless of preimpact crustal thickness or thermal state [Ivanov *et al.*, 2010; Potter *et al.*, 2012b]. The crustal cap is also hotter in basins created by smaller impactors, as such basins retain more shocked crustal material, whereas such material is more readily ejected by larger impactors.

Our finding that the crustal structure following transient crater collapse closely matches that of the contemporary crustal structure inferred from gravity and topography observations (Figures 2h and 3h) implies that there was no substantial addition (i.e., more than a few kilometers) of new crust from differentiation of the melt pool as it cooled. This result is consistent with a shallow mantle that was already depleted of crust-forming material during the initial differentiation of the lunar crust and mantle. It is also possible that differentiation may not have had a major influence on gravity and topography because it involved no net change in mass, although lower-density material would have been brought closer to the surface. If the post-crater-collapse crust were

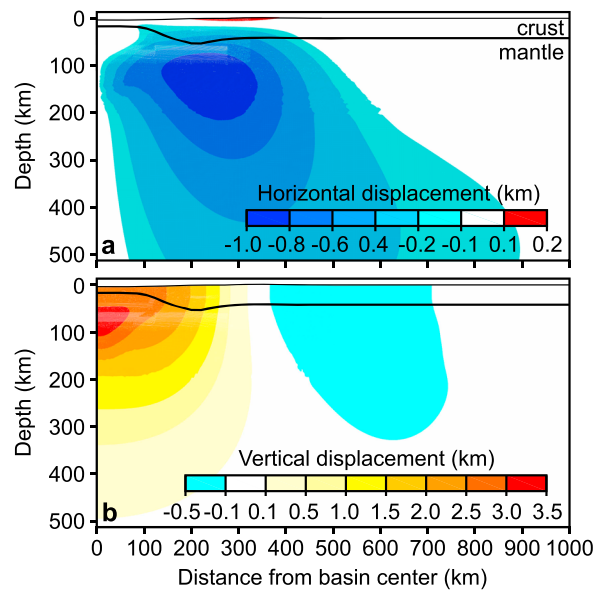


Figure 14. FEM calculations of (a) horizontal and (b) vertical displacements of the Freundlich-Sharonov basin due to cooling and isostatic adjustment following transient crater collapse (last frame from Figure 10). See text for the discussion of best fitting FEM parameters.

These figures show steady-state conditions after 300 Myr of mantle relaxation, although most isostatic adjustment takes place within the first 30 Myr. As expected, because of postcollapse pressure gradients (Figure 8), viscous mantle is driven toward the basin center (Figure 14a). Flow is greatest beneath the crustal collar where postcollapse overburden pressure was minimized (subisostatic). By axisymmetry, no horizontal flow can occur at the basin center. Mantle at the basin center must therefore flow vertically, which combined with a free surface leads to uplift. Uplift is maximized at the basin center; the Freundlich-Sharonov basin rises almost 3 km (Figure 14b). The crustal collar rises almost 2 km, whereas modest subsidence occurs for the ejecta blanket outside the basin, where postcollapse overburden pressures were highest (superisostatic). A comparison of the final predicted topography (Figure 2f and Figure 4) with observed topography shows it to cut midway through shorter-wavelength variations interpreted to be associated with fault scarps. As no faults are considered in the modeling, this outcome is perhaps the best match that such a model is likely to achieve.

The calculated free-air gravity anomaly from this final predicted state (Figure 2b) of the Freundlich-Sharonov basin compares well with the observed anomaly. The model slightly underpredicts the gravity in the region 100–150 km from the basin center and slightly overpredicts the gravity 200–250 km from the basin center. These radial ranges correspond to those in which the topography is underpredicted and overpredicted, respectively, suggesting that the predicted free-air anomaly is also the best match to the data that should be expected for a model that does not incorporate fault scarps. This result is confirmed by the very close match of the predicted and observed Bouguer gravity anomaly (Figure 2d), for which the influence of the fault scarps on the gravity signature is largely absent.

Despite the greater isostatic forces (lower pressure) beneath the crustal collar compared with the mantle beneath the basin interior following transient crater collapse, the crustal collar rises about a kilometer less during isostatic adjustment. This difference is because of the mechanical continuity that was established between the inner and outer basin as the region cooled and a thick lithosphere (which we define by a viscosity greater than 10^{24} Pa s) developed over the melt pool. Figure 15 shows the development of this lithosphere as a function of time after collapse. By 0.3 Myr, a thin (7 km thick) lithosphere has already developed over the melt pool (Figure 15b). By 15 Myr, the lithosphere has reached 25 km thickness, but it will add only another 15 km to its thickness over the next 275 Myr because cooling near the surface occurs relatively rapidly after collapse but then slows markedly. Note that the lithosphere (Figure 15f) eventually thickens under the basin due to a steady-state temperature that is lower than for surrounding areas because of basin topography.

and Humorum basins must have experienced uplift following transient crater and subsidence of ejecta topography outside the basins. This finding is consistent with the aforementioned subisostatic state of the inner basin and superisostatic state of the outer ejecta region, and potentially the cooling of the melt pool. The outcomes of cooling and isostatic adjustment subsequent to transient crater collapse are computed using our finite element models, the results of which are described next.

4.2. Finite Element Model Results

Finite element model results show that isostatic forces are sufficient to drive uplift of the basin and subsidence of ejecta topography from their postcollapse configuration into their contemporary forms. Calculated horizontal and vertical deformation for the Freundlich-Sharonov basin following cooling and isostatic adjustment is shown in Figure 14. These

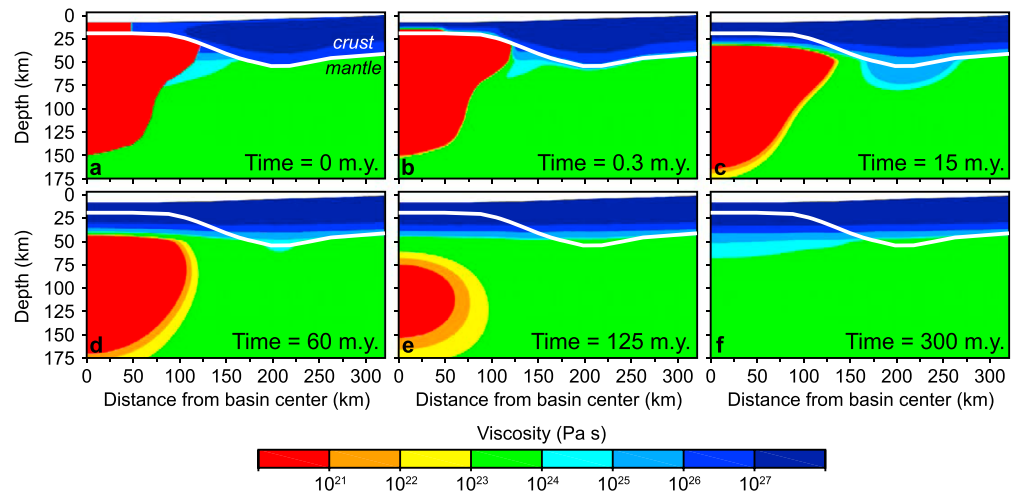


Figure 15. Calculated time series of the effective viscosity beneath the Freundlich-Sharonov basin during cooling following transient crater collapse. For the model shown, the flow law is that of dry diabase deforming under a strain rate of 10^{-16} s^{-1} for a temperature field that cools conductively from the thermal structure shown in Figure 10f.

In our best fitting model for Freundlich-Sharonov basin, the lithosphere over the melt pool develops rather quickly compared with isostatic adjustment. As a result, isostatic forces that drive the crustal collar upward concomitantly lift the inner basin, raising it above isostatic equilibrium. This superisostatic condition

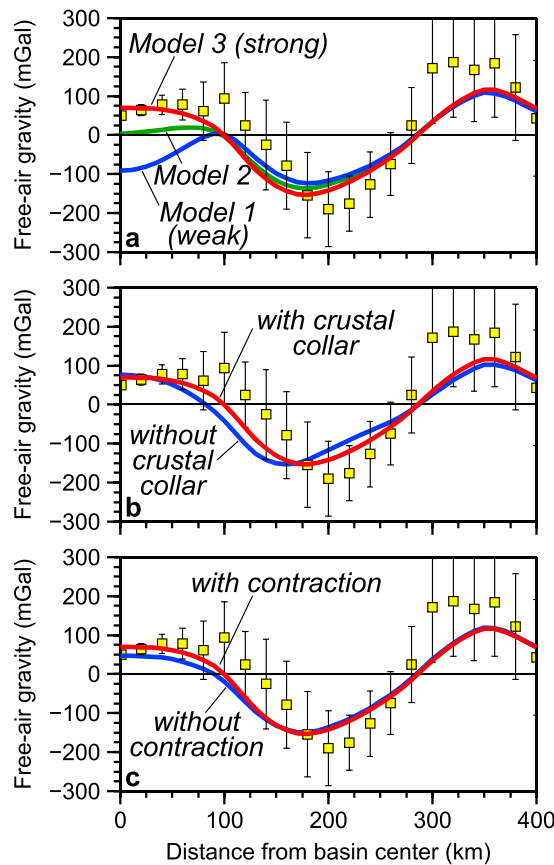


Figure 16. Calculated free-air gravity anomaly for the Freundlich-Sharonov basin as a function of (a) viscosity structure, (b) the existence of a crustal collar, and (c) the contraction of the melt pool during cooling. Models 1, 2, and 3 in Figure 16a are shown in Figure 9.

occurs when the viscosity structure becomes relatively strong as temperatures cool (model 3 or model 4 in Figure 9). Figure 16a shows the calculated free-air gravity anomaly for the Freundlich-Sharonov basin following isostatic adjustment as a function of rheologic strength. The decrease in the free-air gravity anomaly with weaker rheologies results from a thinner lithosphere developing before substantial isostatic uplift occurs. As a result, uplift of the basin center does not gain as much of an assist from the rise in the outer basin. For the stronger rheologies (models 3 and 4), the center of the Freundlich-Sharonov basin rises 2800 m due to isostatic adjustment, but it rises only 1800 m or 1000 m for moderate (model 2) and weak (model 1) rheologies, respectively, resulting in lower free-air gravity. These results suggest that the average viscosity structure for the lunar upper mantle throughout the isostatic process is no less than $\sim 10^{23} \text{ Pa s}$. Such a rheology leads to a situation in which cooling occurs more rapidly than isostatic adjustment, a necessary condition for mascon basins to form.

Our results suggest that the evolution of the free-air anomaly at the center of mascon basins is strongly tied to isostatic adjustment of the outer basin through the developing lithosphere. The outer basin consists of both

depressed topography following transient crater collapse as well as the crustal collar, both of which are subsostatic structures. We can examine the relative contributions of these two components by removing the crustal collar from the model, a step accomplished by changing the density of any crust deeper than 40 km (the preimpact crustal thickness) in the Freundlich-Sharonov model to the density of mantle material. Figure 16b shows that if a thickened crustal collar had never formed, the free-air anomaly of the basin would be only modestly changed from the model with the crustal collar. Recall that the mascon at the basin center requires the assist (through lithospheric continuity) from uplift of the outer basin. These results suggest that the depressed topography is more important than the crustal collar in driving isostatic uplift of the outer basin. This result is not surprising since the density contrast of lowered elevations is equal to the crustal density (i.e., 2550 kg/m^3), whereas the density contrast of the crustal collar is the difference between mantle and crustal densities ($\sim 700 \text{ kg/m}^3$). This is not to say that the formation of a crustal collar is not an integral part of the evolution of these basins. The hydrocode calculations suggest that the development of low elevation following transient crater collapse is closely tied to the development of a crustal collar. So both are important in the evolution of large impact basins.

Another factor to be considered in the formation of a mascon basin is the role of thermal contraction of a cooling melt pool. Contraction would pull material inward toward the melt pool from all directions, including the free surface above and deeper mantle below. If the surface does not subside as a result of contractional forces and only the mantle rises, then the free-air anomaly will increase and a mascon basin may form. This idea was successfully tested by *Melosh et al.* [2012] with an analytical model and a perfectly rigid crust. The question remained with that model as to whether a finite elastic strength would be sufficient to prevent substantial subsidence of the surface during contraction, negating the formation of a mascon. Whereas our model indeed shows that an elastic lithosphere is sufficient to develop a mascon, the development of the mascon is primarily the result of isostatic adjustment. To show the influence of contraction on our solution, we ran a model in which contraction was omitted by setting the coefficients of thermal expansion to zero. Results show that by ignoring contraction, the free-air anomaly for the Freundlich-Sharonov basin center was reduced by only 23 mGal (Figure 16c). This outcome is because the increase in the free-air gravity contributed by rising mantle during contraction was offset by $\sim 250 \text{ m}$ of contraction-induced subsidence. The relative unimportance of contraction of the melt pool during cooling likely applies only to basins the size of Freundlich-Sharonov and Humorum (40-km-diameter impactor) and smaller. Larger impactors would lead to larger melt pools as well as higher impact temperatures, potentially increasing the influence of melt pool contraction on the postcollapse evolution of these basins.

Because Humorum contains thick mare basalt deposits, we do not have direct observational constraints on gravity and topography of the unfilled, post-collapse configuration. Given that Humorum and Freundlich-Sharonov basins are of similar size—indicated by the similar diameters of their crustal collars—we assume that the same parameters that controlled the evolution of the Freundlich-Sharonov basin (with the exception of different preimpact crustal thickness) apply to that of the Humorum basin. From these assumptions, we calculated the premare gravity and topography signature of the Humorum basin, shown in the right column of Figure 3. As expected, the calculated free-air gravity and topography of the unfilled Humorum basin greatly underpredict the observed gravity and topography within the inner basin (Figures 3b and 3f). Note that the calculation predicts that Humorum would have been a mascon basin even in the absence of mare volcanism, in support of previous findings [*Neumann et al.*, 1996; *Wieczorek and Phillips*, 1999]. In contrast, the predicted Bouguer gravity of the unfilled basin reasonably matches that of the observed gravity. This result is not that surprising because the Bouguer correction removes most topographic contributions to gravity (given an appropriate assumed distribution of crustal density). The major difference between the Bouguer anomalies of a basin with and without mare basalt is therefore the relatively small difference between the density of the mare material (assumed here to equal the density of the mantle) and the density of the crust. Thus, although the addition of mare basalt deposits has little effect on the Bouguer anomaly, their contribution to the free air gravity anomaly can be substantial.

In our calculations, the Humorum basin floor prior to mare volcanism sits $\sim 2 \text{ km}$ below the observed mare surface. We explored several possible thicknesses for the mare deposits, seeking the configuration that, combined with the subsidence of this surface load, would lead to the observed topography. As our calculations suggest that most isostatic compensation is completed within a few tens of millions of years following

impact, we assumed that mare material was emplaced in an isostatically compensated basin. We found that the present topography is consistent with a mare thickness of 2.4 km at the basin center, tapering to zero thickness at a distance of 200 km from the basin center. The additional 400 m of mare thickness at the basin center is equivalent to the amount of subsidence caused by the mare load. This configuration of mare fill leads to a calculated free-air anomaly (Figure 3b) very close to that observed. The addition of the mare had only a minor influence on the calculated Bouguer gravity anomaly, consistent with the discussion above that the Bouguer calculation is fairly insensitive to this volume of mare material.

5. Conclusions

We have combined hydrocode and finite element models to simulate the formation of the Freundlich-Sharonov and Humorum lunar basins from impact to contemporary form. Our models successfully predict free-air and Bouguer gravity anomalies, topography, and crustal thickness that are in good agreement with observations from GRAIL and LOLA. The goodness of fit across these four sets of constraints, combined with the plausibility of the model parameters, leads to a high level of confidence that these models are accurate representations of the processes that govern basin evolution on the Moon. These processes include impact, transient crater collapse, cooling, and isostatic adjustment.

Given an impact velocity of 15 km/s and vertical or near-vertical impact, our models enable us to infer that a ~40-km-diameter impactor was responsible for these basins. If the impact velocity were higher, the impactor diameter would have been proportionally less, and vice versa. The analysis suggests that the preimpact crust and mantle were sufficiently weak so as to permit a vigorous collapse of the transient crater following impact that was sufficient to enable a crustal cap to flow back over and cover the inner basin. Numerically, this process occurs only if the preimpact thermal gradient was fairly high (reaching a temperature of 1300 K by 40 km depth). The analysis suggests preimpact crustal thickness values of 40 and 30 km for the Freundlich-Sharonov and Humorum basins, respectively. These values are consistent with the inferred current thickness of the farside and nearside crust that surrounds the Freundlich-Sharonov and Humorum basins, respectively. In addition, the model suggests a mare thickness of 2.4 km at the center of the Humorum basin.

There are two keys to the development of a mascon basin. The first is that transient crater collapse leaves a basin that is strongly subsisostatic, supported by the frictional strength of the crust and a viscoelastic mantle that requires time to relax. The second is that the inner basin becomes mechanically coupled to the outer basin as cooling produces a new lithosphere, so that both the inner and outer parts of the basin rise together in response to isostatic forces. Isostatic forces generally cannot lift a structure above isostatic equilibrium. However, this coupling across the basin structure enables the inner basin to obtain additional uplift from the strong isostatic forces beneath the surrounding crustal collar. Our results suggest that this coupling will occur only if isostatic adjustment is sufficiently slow that a strong lithosphere has time to develop over the melt pool. This constraint is satisfied if the effective viscosity of the lunar mantle is at least 10^{23} Pa s. The viscosity of the mantle could, however, be lower if cooling near the top of the melt pool occurs faster than that inferred by the modeling. Such rapid cooling is likely given that the model does not take into account that convection within the melt pool decreases the cooling time.

Model results suggest that for basins the size of Freundlich-Sharonov and Humorum (crustal collar located ~200 km from the basin center), contraction associated with the cooling melt pool is not a critical factor in the formation of a mascon. This result follows because any increase in free-air gravity caused by drawing mantle toward the basin center is offset by subsidence of the surface. Our models suggest that even the development of a lithosphere above the melt pool does not prevent such subsidence. One cannot conclude, however, that such contraction would not play a more important role for larger basins, where the size of the melt pool after impact would be substantially larger.

Once an impactor diameter, lunar thermal gradient, and crustal thickness are chosen for the initial conditions at impact in the hydrocode calculations, finite element solutions for the development of a mascon basin can be found that are a good match to observations. Alternative conditions following impact and transient crater cavity collapse, such as a different surface topography or variations in the assumed density of crust or mantle, lead to trade-offs with the isostatic forces such that the final predicted gravity and topography of these basins are only modestly changed. The basic finding of substantial isostatic

adjustment following collapse is robust, and the wealth of constraints enables fine-tuning of FEM parameters. In the end, we are able to relate the contemporary measurements of the gravity signature and topography of the Freundlich-Sharonov and Humorum basins to the tectonic conditions that prevailed early in the history of the Moon.

Acknowledgments

We gratefully acknowledge the developers of iSALE (www.isale-code.de/projects/ISALE), including Gareth Collins, Kai Wünnemann, Dirk Elbeshausen, and Boris Ivanov. We thank Boris Ivanov, an anonymous reviewer, Gareth Collins, and another Associate Editor for their constructive comments on an earlier draft. The GRAIL mission is supported by the NASA Discovery Program and is performed under contract to the Massachusetts Institute of Technology and the Jet Propulsion Laboratory. The Lunar Reconnaissance Orbiter LOLA investigation is supported by the NASA Science Mission Directorate under contract to the NASA Goddard Space Flight Center and Massachusetts Institute of Technology. Data from the GRAIL and LOLA missions have been archived in the Geosciences Node of the NASA Planetary Data System.

References

- Amsden, A. A., H. M. Ruppel, and C. W. Hirt (1980), SALE: A simplified ALE computer program for fluid flow at all speeds, *LANL Rep. LA-8095*, 101 pp., Los Alamos National Laboratory, Los Alamos, N. M.
- Andrews-Hanna, J. C. (2013), The origin of the non-mare mascon gravity anomalies in lunar basins, *Icarus*, *222*, 159–168.
- Benz, W., A. G. W. Cameron, and H. J. Melosh (1989), The origin of the Moon and the single-impact hypothesis III, *Icarus*, *81*, 113–131.
- Bottinga, Y., and D. F. Weill (1970), Densities of liquid silicate systems calculated from partial molar volumes of oxide components, *Am. J. Sci.*, *269*, 169–182.
- Budney, C. J., and P. G. Lucey (1996), Basalt thickness in Mare Humorum: New method and results, *Lunar Planet. Sci.*, *27*, 179–180.
- Collins, G. S., H. J. Melosh, and B. A. Ivanov (2004), Modeling damage and deformation in impact simulation, *Meteorit. Planet. Sci.*, *39*, 217–231.
- Davison, T. M. (2011), Numerical modelling of heat generation in porous planetesimal collisions, PhD thesis, Imperial College London, London, U. K.
- Evans, A. J., M. T. Zuber, B. P. Weiss, and S. M. Tikoo (2014), A wet, heterogeneous lunar interior: Lower mantle and core dynamo evolution, *J. Geophys. Res. Planets*, *119*, 1061–1077, doi:10.1002/2013JE004494.
- Ito, T., and R. Malhotra (2006), Dynamical transport of asteroid fragments from the ν_6 resonance, *Adv. Space Res.*, *38*, 817–825.
- Ivanov, B. A., H. J. Melosh, and E. Pierazzo (2010), Basin-forming impacts: Reconnaissance modeling, in *Large Meteorite Impacts and Planetary Evolution IV, Spec. Pap.*, vol. 465, edited by R. L. Gibson and W. U. Reimold, pp. 29–49, Geol. Soc. of Am., Boulder, Colo.
- Kiefer, W. S., R. J. Macke, D. T. Britt, A. J. Irving, and G. J. Consolmagno (2012), Regional variability in the density of lunar mare basalts and implications for lunar gravity modeling, *Lunar Planet. Sci.*, *43*, abstract 1642.
- Lange, R. L., and I. S. E. Carmichael (1990), Thermodynamic properties of silicate liquids with emphasis on density, thermal expansion and compressibility, *Rev. Mineral. Geochem.*, *24*, 25–64.
- Le Feuvre, M., and M. A. Wieczorek (2008), Nonuniform cratering of the terrestrial planets, *Icarus*, *197*, 291–306.
- Le Feuvre, M., and M. A. Wieczorek (2011), Nonuniform cratering of the Moon and a revised crater chronology of the inner Solar System, *Icarus*, *214*, 1–20.
- Mackwell, S. J., M. E. Zimmerman, and D. L. Kohlstedt (1998), High-temperature deformation of dry diabase with application to tectonics on Venus, *J. Geophys. Res.*, *103*, 975–984, doi:10.1029/97JB02671.
- Melosh, H. J. (1989), *Impact Cratering: A Geologic Process, Oxford Monographs on Geology and Geophysics Ser.*, *11*, 253 pp., Oxford Univ. Press, New York.
- Melosh, H. J., D. M. Blair, and A. M. Freed (2012), Origin of superisostatic anomalies in lunar basins, *Lunar Planet. Sci.*, *43*, abstract 2596.
- Melosh, H. J., et al. (2013), The origin of lunar mascon basins, *Science*, *340*, 1552–1555, doi:10.1126/science.1235768.
- Miljković, K., M. A. Wieczorek, G. S. Collins, M. Laneuville, G. A. Neumann, H. J. Melosh, S. C. Solomon, R. J. Phillips, D. E. Smith, and M. T. Zuber (2013), Asymmetric distribution of lunar impact basins caused by variations in target properties, *Science*, *342*, 724–726, doi:10.1126/science.1243224.
- Muller, P. M., and W. L. Sjogren (1968), Mascons: Lunar mass concentrations, *Science*, *161*, 680–684.
- Neumann, G. A., M. T. Zuber, D. E. Smith, and F. G. Lemoine (1996), The lunar crust: Global structure and signature of major basins, *J. Geophys. Res.*, *101*, 16,841–16,863, doi:10.1029/96JE01246.
- Pierazzo, E., and H. J. Melosh (2000), Melt production in oblique impacts, *Icarus*, *145*, 252–261.
- Potter, R. W. K. (2012), Numerical modeling of basin-scale impact crater formation, PhD thesis, Imperial College London, England.
- Potter, R. W. K., D. A. Kring, G. S. Collins, W. S. Kiefer, and P. J. McGovern (2012a), Estimating transient crater size using the crustal annular bulge: Insights from numerical modeling of lunar basin-scale impacts, *Geophys. Res. Lett.*, *39*, L18203, doi:10.1029/2012GL052981.
- Potter, R. W. K., G. S. Collins, W. S. Kiefer, P. J. McGovern, and D. A. Kring (2012b), Constraining the size of the South Pole-Aitken basin impact, *Icarus*, *220*, 730–743.
- Potter, R. W. K., D. A. Kring, G. S. Collins, W. S. Kiefer, and P. J. McGovern (2013), Numerical modeling of the formation and structure of the Orientale impact basin, *J. Geophys. Res. Planets*, *118*, 963–979, doi:10.1002/jgre.20080.
- Smith, D. E., et al. (2010), Initial observations from the Lunar Orbiter Laser Altimeter (LOLA), *Geophys. Res. Lett.*, *37*, L18204, doi:10.1029/2010GL043751.
- Spudis, P. D., D. J. P. Martin, and G. Kramer (2014), Geology and composition of the Orientale basin impact melt sheet, *J. Geophys. Res. Planets*, *119*, 19–29, doi:10.1002/2013JE004521.
- Stewart, S. T. (2011), Impact basin formation: The mantle excavation paradox resolved, *Lunar Planet. Sci.*, *42*, abstract 1633.
- Taylor, S. R. (1982), *Planetary Science: A Lunar Perspective*, 401 pp., Lunar and Planetary Institute, Houston, Tex.
- Wieczorek, M. A., and R. J. Phillips (1999), Lunar multiring basins and the cratering process, *Icarus*, *139*, 246–259.
- Wieczorek, M. A., et al. (2013), The crust of the Moon as seen by GRAIL, *Science*, *339*, 671–675, doi:10.1126/science.1231530.
- Wünnemann, K., G. S. Collins, and H. J. Melosh (2006), A strain-based porosity model for use in hydrocode simulations of impacts and implications for transient crater growth in porous targets, *Icarus*, *180*, 514–527.
- Wünnemann, K., G. S. Collins, and G. R. Osinski (2008), Numerical modeling of impact melt production in porous rocks, *Earth Planet. Sci. Lett.*, *269*, 530–539.
- Zuber, M. T., et al. (2013), Gravity field of the Moon from the Gravity Recovery and Interior Laboratory (GRAIL) mission, *Science*, *339*, 668–671, doi:10.1126/science.1231507.